Additive Manufacturing 94 (2024) 104504

Contents lists available at ScienceDirect

Additive Manufacturing

journal homepage: www.elsevier.com/locate/addma

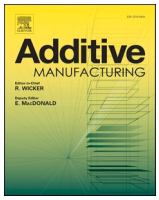

Prediction of spatter-related defects in metal laser powder bed fusion by analytical and machine learning modelling applied to off-axis long-exposure monitoring

Nicolò Bonato *, Filippo Zanini, Simone Carmignato

Department of Management and Engineering, University of Padua, Vicenza, Italy

ARTICLE INFO

Keywords:
Laser powder bed fusion
In-process monitoring
Image processing
Machine learning
Data correlation
X-ray computed tomography

ABSTRACT

Laser powder bed fusion of metals is increasingly used for fabricating complex parts requiring good mechanical properties. Simultaneously, researchers in the field are intensifying the efforts to reduce defects, such as internal porosities, which hinder a wider industrial adoption of this technology, urging process monitoring to a pivotal role in defect identification and mitigation. Therefore, understanding the correlation between in-process monitoring signals and post-process actual defects is fundamental to taking informed decisions and potential corrective actions during the process. This work focuses on developing models to predict spatter-related defects from specific process signatures detected through off-axis long-exposure imaging. Layer-wise images were properly aligned with corresponding cross-sections from tomographic reconstructions to investigate the relationship between spatter-related signatures and actual defects measured by X-ray computed tomography. This relationship was used as a knowledge basis to develop an analytical image-processing approach and a machine learning-based methodology, which were then compared in terms of their correlation performances. The advantages and limitations of both methods are discussed in the paper. Both approaches led to promising results in the prediction of lack-of-fusion defects caused by spatters, with the machine learning approach showing a prediction accuracy in the order of 90 % for defects with equivalent diameter above 90 μm, while the analytical model needed equivalent diameters larger than 130 μm to reach a prediction accuracy in the order of 80 %. Furthermore, the machine learning method led to strong results regarding early defect detection, with most of the investigated defects properly predicted by analysing two consecutive layers after the signature detection.

1. Introduction

Additive manufacturing (AM) technologies have emerged as innovative solutions for fabricating components with complex geometries for several applications, spanning industries such as biomedical, aerospace, automotive, tooling, and consumer goods [1]. In particular, laser-based powder bed fusion of metals (PBF-LB/M) offers unprecedented advantages in terms of design freedom, material buy-to-fly ratio, weight reduction, and mechanical performances. However, ensuring the stringent quality standards required across various applications remains a significant challenge, for example, due to the susceptibility of the fabricated parts to flaws, including internal porosities, which poses a considerable barrier to achieving consistent and reliable mechanical properties [2]. Despite significant efforts to optimize process parameters, the intrinsic variability in mechanical properties persists due to the difficult-to-predict nature of defects formed during PBF-LB/M fabrication [3]. Notably, lack-of-fusion voids – distinguishable by their characteristic irregular shapes and the presence of partially melted entrapped powder particles – significantly impact part resistance and often lead to fatigue failures at the material-pore interface [4]. The quest for a comprehensive understanding of the specific causes behind these defects has prompted several investigations into the complex relationship between PBF-LB/M process anomalies and the resulting part defects. Pioneering studies reported in the literature highlighted the importance of leveraging reliable measurements to harness the extensive in-process data generated by sensors with varying operating principles integrated into additive manufacturing systems [5,6]. Indeed, the iterative layer-wise nature of AM processes provides an ideal framework for sensors integration, offering valuable insights into defect formation at early stages and paving the way for closed-loop control systems [7].

* Correspondence to: Stradella San Nicola 3, Vicenza 36100, Italy.
E-mail address: nicolo.bonato@phd.unipd.it (N. Bonato).

https://doi.org/10.1016/j.addma.2024.104504
Received 12 July 2024; Received in revised form 25 September 2024; Accepted 18 October 2024
Available online 19 October 2024

In recent years, in-process monitoring solutions have witnessed significant exploration in the realm of PBF-LB/M, employing various sensors and data types [8]. In particular, some approaches rely on the acquisition of high-resolution images in visible wavelengths, showing promising results for the identification of surface-visible anomalies in the powder bed after the recoating operation [9], as well as in the geometry of the printed slices after the laser action [10]. However, the visible wavelength range highly depends on lighting conditions, thus motivating the use of different wavelengths for in-process monitoring. For instance, near-infrared cameras were investigated for the identification of process signatures related to large lack-of-fusion defects [11]. Near-infrared in-process monitoring has also been used to detect spatter particles [12], which are ejected from the melt pool and often drop onto other regions of the powder bed, acting as potential seeds for lack-of-fusion porosities [13].

In image-based in-process monitoring approaches, one or a few images are typically gathered per layer. Other solutions focus on acquiring in-situ data closer to the local PBF-LB/M process dynamics, resulting in significantly more data per layer. High-temporal resolution infrared cameras capture temperature evolution over time, identifying anomalies from improper cooling gradients [14], while photodiodes are used in melt pool monitoring and show potential for identifying signals leading to keyhole porosities [15].

The above-mentioned studies contributed to the unravelling of interesting insights from in-process signals, while the large amount of data generated from each build and the various nature of the acquired signals motivate the recent attempts to integrate artificial intelligence (AI) algorithms in the analysis of PBF-LB/M monitoring data. Despite challenges regarding their physical interpretability and actual reliability [16], AI-based approaches, leveraging machine learning (ML) or deep learning (DL) models, can facilitate real-time feature extraction and anomaly classification [17–19]. These methods can potentially enable the detection of defects at their early onset stages, as well as the proactive intervention during fabrication for real-time defects healing [20].

The present study aims at developing and evaluating prediction models for defect formation, to be applied during the PBF-LB/M fabrication. Particular attention is given to the feasibility of real-time implementation of the models to enable feedback control actions on the process. The prediction specifically targets the formation of spatter-related porosities, which can drastically affect the mechanical properties of industrial components and whose potential real-time detection has not been thoroughly investigated so far. A fundamental aspect to consider when modelling relations involving in-process monitoring data is the accuracy in the alignment with post-process data, serving as a reference on the actual defect formation. In fact, validating monitoring solutions and advancing the understanding of PBF-LB/M processes lies heavily on determining reliable reference data linking in-process anomalies to actual defects. In this context, X-ray computed tomography (CT) emerges as a powerful defect analysis and measurement tool, providing holistic evaluations of external and internal geometry and defects [21]. Post-process CT measurements of laser powder bed fusion metal parts can provide reference data crucial for the validation of in-process monitoring solutions, provided that the alignment between compared datasets is accurate. However, the alignment between in-process and post-process datasets is not trivial, since parts are commonly affected by deformations occurring between in-situ data gathering and CT analyses. A new alignment solution was recently proposed to improve the comparison between in-process monitoring data and post-process CT data, accounting for both shrinkage and local distortions [22]. This approach specifically enables the correlation of porosities with an equivalent diameter greater than 50 μm to corresponding regions in the in-process data, with a probability of over 90 %.

The capabilities of in-process long-exposure imaging combined with advanced algorithms to detect lack-of-fusion pores caused by undesired spatter particles are therefore investigated in this work, by correlation of process events and CT reference data of actual defects leveraging the above-mentioned alignment approach. In particular, two different correlation approaches are described and implemented, one based on analytical methods applied through sequential image processing operations, and the other based on image convolution and machine learning. Results are focused on evaluating the model performances and comparing the two approaches, deriving insights for their respective fields of application. Specifically, the correlation performance of the two approaches is examined with reference to the number of consecutive layers needed to take a decision, thereby providing relevant information for real-time accurate and early defect detection. The developed methodologies also demonstrate the effective use of low-cost and machine-agnostic hardware solutions, such as long-exposure optical cameras, for predicting lack-of-fusions caused by spatter particles.

The paper presents material and methods in Section 2, which deals with the fabrication of the samples, the in-process monitoring setup and acquisition technique, and the post-process CT analyses with the related alignment methodology. Section 3 describes the developed analytical approach based on image processing and the machine-learning-based approach proposed for classifying each signature detected during the process. Results of both approaches are presented in Section 4, focusing specifically on the dimensions of the detectable defects and the model earliness.

2. Material and methods

This section covers the fabrication of the samples by PBF-LB/M, describing particularly the used materials and process parameters (Section 2.1), as well as the in-process monitoring system (Section 2.2), metrological X-ray CT-based method for obtaining the reference data (Section 2.3), and the methodology implemented for the data alignment (Section 2.4).

2.1. PBF-LB/M samples fabrication

The design presented in a previous work [23], specifically conceived to enhance the accuracy of the alignment between in-process monitoring data and post-process CT data, was exploited in this work to produce parts made of Ti6Al4V and H13 tool steel using the PBF-LB/M machine Sisma MYSINT 100 (Sisma SpA, Italy). Working with data from two different materials was done with the aim of improving the generalization capabilities of the developed defect prediction methods.

The main process parameters adopted for each material are listed in Table 1.

A meander scanning strategy with 67 degrees of rotation between following layers was chosen for both materials. To aid consequent CT scans and post-process analyses, the samples were directly printed without supports on removable inserts produced by high-precision machining, belonging to a new building platform shown in Fig. 1a. Building platforms made of Ti6Al4V and H13 tool steel were used in the experiments, corresponding to the material being analysed. Both platforms share the same geometry, consisting of a main disk with a nominal diameter of 99 mm and a height of 15 mm. The platforms were manufactured with fine tolerances, using the hole-basis fit system H7/g6 for assembling the inserts [24]. The representation of one insert extracted from the platform with a part produced on top is depicted in Fig. 1b,

Table 1
Process parameters for samples fabricated in Ti6Al4V and H13. P is the laser power, v the scanning speed, h the hatch spacing between adjacent laser tracks, and t the layer thickness.

	Ti6Al4V	H13
P [W]	155	120
v [mm/s]	1200	600
h [mm]	0.110	0.090
t [mm]	0.020	0.020

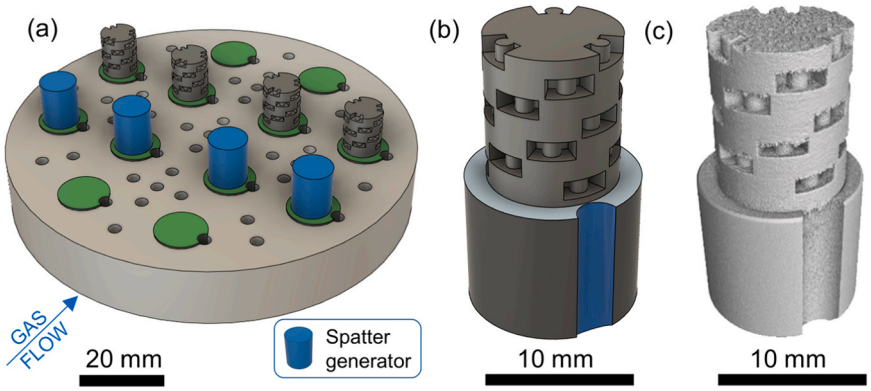

Fig. 1. Positioning of the samples on the building platform for both materials (a), sample-holder with printed sample on its top surface (b) and CT scanned volume of one of the samples fabricated in H13 tool steel (c).

while Fig. 1c shows the CT reconstructed volume as described in Section 2.3. Further details regarding the design and manufacturing of the platform and inserts are documented elsewhere [25].

With the aim to reduce the dross formation on flat down-skin horizontal surfaces [26], the laser power was reduced by 50 % for three consecutive layers before switching back to the nominal value reported in Table 1.

Samples were fabricated as represented in Fig. 1a for both materials, resulting in a total of eight samples analysed. Additional cylindrical samples (hereafter named spatter generators) were interposed between the gas flow outlet and the samples of interest, with the purpose of stimulating the deposition of spatter particles on specific regions.

In particular, the laser scanning order was set to follow the gas flow direction, so that some spatters originating from the cylindrical spatter generators, which are scanned first, drop on regions where the samples of interest are going to be fabricated. A meander scanning with a fixed orientation of scan tracks, parallel to the gas flow direction (shown in Fig. 1a), was chosen to fabricate the spatter generators, which helps conveying the spatter particles in the direction of the monitored samples [27]. Furthermore, the gas flow speed was decreased by 50 % with respect to the commonly used value to decrease the spatters removal rate. It is worth highlighting that, although this strategy may appear unconventional, the overall aim is to increase the number of lack-of-fusion defects caused by spatters (often observed also in case of good job preparation) to improve the statistical significance of the study.

2.2. Off-axis long-exposure monitoring system

The in-process monitoring system used in this work is constituted by an 18 megapixel digital single-lens reflex (DSLR) camera installed outside the PBF-LB/M machine with an off-axis positioning, meaning that the camera sensor is tilted with respect to the building platform. Images are gathered during the fabrication through a long-exposure technique. With this technique, the camera integrates the radiations emitted while the powders are molten, resulting in one image per layer which is representative of the whole scanning path. Specifically, the acquisition time was set so that the whole layer processing is registered, while camera settings (aperture, shutter speed, ISO sensitivity) were tuned to avoid signal saturation in data acquisition. The amount of data to be managed is therefore reduced by the signal integration over time. Moreover, this image acquisition method does not require any lighting source, as opposed to the acquisition of powder bed or printed slice images, where the lighting conditions play a fundamental role in the defects' detection capability [28].

Given the off-axis camera positioning, perspective distortions need to be corrected before analysing the acquired images. The novel building platform illustrated in Fig. 1a was employed to address this step. In fact, the platform comprises several reference holes that provide the actual coordinates in the physical coordinate space. As can be seen from Fig. 1a, the holes cover different areas of the building platform, which allows both a global perspective correction of the entire building platform carried out using the coordinates of all the holes, as well as a local correction limited to a few samples of interest, which can be particularly useful in case of cameras with high spatial resolution and limited field of view. In this work, the reference holes placed close to the monitored samples were exploited to determine a perspective transformation function that is consequently applied to all the images acquired layer-by-layer. The resulting pixel size was equal to 15 μm. Fig. 2a shows an example of a gathered image of one layer, while Fig. 2b shows the same image after the perspective correction. The details about the above-mentioned perspective correction procedure can be found in the work conducted by Zanini et al. [25].

2.3. Post-process X-ray computed tomography

After fabrication, the samples were scanned using a metrological X-ray computed tomography system (MCT225, Nikon Metrology, UK). The system is characterized by a 225 kV micro focus X-ray source with a minimum focal spot size equal to 3 μm, a 2000 × 2000 pixels 16-bit flat-panel detector and a shielding cabinet with temperature control at 20 ± 0.5 °C. Table 2 lists the CT scanning parameters used for the two materials.

The samples were printed on removable inserts as represented in Fig. 1b, to improve their positioning and scanning, reaching a voxel size equal to 7.7 μm after volume reconstruction. An example of volume reconstruction of one of the fabricated samples is shown in Fig. 1c.

A further benefit of fabricating the samples on the platform's inserts relies on the presence of a flat horizontal plane and a notch (see surfaces colour-coded in blue and light blue, respectively, in Fig. 1b). These features enable the establishment of an accurate reference system for the samples in the CT three-dimensional coordinate space, defining the basis for applying the data alignment methodology discussed in Section 2.4.

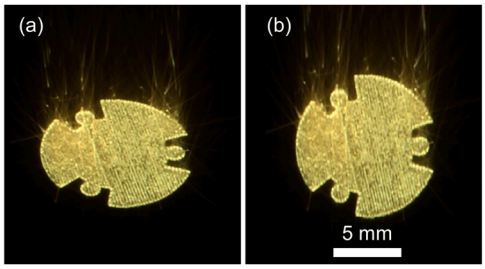

Fig. 2. Acquisition of a long-exposure image of one of the fabricated samples (a) and outcome from the same image after performing the perspective correction (b).

Table 2
CT scanning parameters for Ti6Al4V and H13 manufactured samples.

	Ti6Al4V	H13
Voltage [kV]	200	210
Current [μA]	35	33
Power [W]	7.0	6.9
Exposure time [ms]	1420	2000
Frames per projection	1	1
Nr. of projections	2000	2000
Physical filter material	Cu	Cu
Physical filter thickness [mm]	0.1 mm	0.25 mm

The reconstructed volumes were then analysed by using the software VG Studio MAX (Volume Graphics GmbH), where a local-adaptive surface determination was performed to discriminate the material from the background. Then, a porosity analysis was also conducted, in order to obtain CT data regarding actual defects present in each sample after the fabrication.

Results of the porosity analysis revealed a significant presence of defects within the bulk of the layer, while limited porosity was found near the surface of the samples. Thousands of pores were analysed throughout the research, with size distribution ranging from 40 to 300 μm in equivalent diameter.

2.4. Data alignment methodology

The context of PBF-LB/M monitoring requires reliable reference data to be successful in determining potential defects through analysing the process-related data. Hence, the accurate alignment between in-process and post-process CT data is fundamental for the establishment of robust correlations and models. However, the data alignment is often hindered by typical part deformations occurring during and/or after the fabrication. These deformations commonly lead to misalignments between the in-process monitoring dataset, consisting of layer-by-layer acquisitions along the building direction, and the post-process CT volume, representative of the after-build condition, which typically deviates from the nominal part geometry.

Therefore, the deformations modelling methodology already presented in [22], which enables the effective alignment and comparison between in-process monitoring data and CT post-process measurements, was applied to the fabricated samples.

By following this approach, local deformations and shrinkages can be properly grasped and considered in the alignment procedure, as the method allows the extraction of aligned CT cross-sections that can be compared to the corresponding layer-wise image gathered during manufacturing. As a result, the probability of accurately correlating porosities with an equivalent diameter above 50 μm to corresponding regions in the in-process data is over 90 %. More details on the deformations modelling methodology, as well as on its experimental application, are reported in [22].

3. Prediction of spatter-related defects by long-exposure in-process monitoring

This section presents two different approaches (analytical and ML-based approach) for analysing the in-process data gathered using the long-exposure technique to predict the presence of actual defects caused by the undesired presence of spatter particles in the fabricated parts. In particular, Section 3.1 presents the analytical approach, while Section 3.2 describes the approach based on machine learning.

3.1. Analytical approach

Upon the data alignment has been performed as described in Section 2.4, the two datasets (long-exposure monitoring data and post-process CT data) are compared to investigate the chance of building models for correlating the outlier events detected through the long-exposure images and the corresponding defects resulting from CT porosity analyses. Specifically, the defects under investigation consist of porosities that appear to partially circumscribe large solid round particles, as illustrated in Fig. 3. In long-exposure images, for both materials, orange spots were frequently observed in regions where an internal porosity was detected in the CT reconstruction, as shown in Fig. 4(a-d).

The solid particles shown in Fig. 3 originate from spatter formations that drop onto specific locations of the powder bed, preventing effective powder melting in subsequent layers and increasing the risk of lack-of-fusion pores. An orange spot in the in-process image as that of Fig. 4a can be associated with a heat accumulation in the same location, as the heat carried by the glowing spatter dissipates slowly.

However, some of the detected orange spots were not observed to be linked to actual lack-of-fusion defects, nor to other kinds of flaws. The long-exposure images acquired on the layers produced after the orange spot observations revealed that, for those spots determined correlated to actual lack-of-fusion pores, the scan tracks are frequently curved, and not straight as expected in normal processing conditions. The cause of curved tracks was identified in the out-of-plane deviation of the laser occurring when encountering a spatter particle on its path, considering that spatter particles are frequently larger than 100 μm in size [12], hence at least 5 times the nominal layer thickness of 20 μm. Curved tracks are visible in the example reported in Fig. 4(a-c). Fig. 4d shows another example of a relatively large orange spot that can be in principle categorized as an outlier event. Despite this clear signal, the scan tracks do not show any relevant curvature in the following layers (see for example Fig. 4e), and the extracted CT cross-section of the corresponding region does not show any defect, as can be noticed in Fig. 4f.

These observations constitute the basis for the development of an analytical model based on image processing, aiming at classifying the candidate long-exposure outliers into events leading or not leading to defects. The approach explained in the following is implemented to quantitatively evaluate the performances of the algorithm by introducing metrics related to false positives, i.e., signals not leading to porosities, as well as to true positives, i.e., signals leading to actual defects within the part.

The analytical image processing method, implemented in MATLAB, consists of a first identification of orange spots as process signatures within the layer-wise long-exposure images, i.e., potential sites for defects onset.

In order to detect these spots, the acquired images are converted from the *RGB* (Red-Green-Blue) domain to the *HSV* (Hue-Saturation-Value) domain, where the *H-channel* represents the hue colour space, the *S-channel* is related to the pixel saturation and the *V-channel* to the pixel intensity value. A histogram in the *HSV* domain of a region of interest

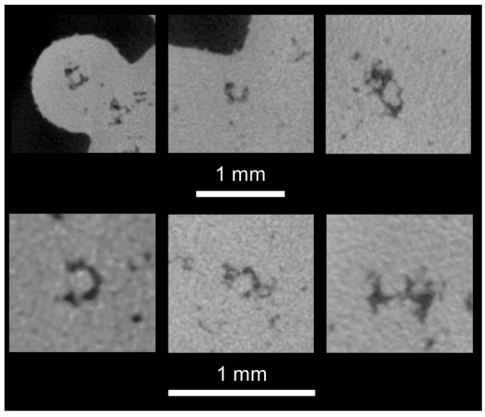

Fig. 3. Examples of transversal CT cross-sections of the fabricated samples, showing typical lack-of-fusion porosities surrounding solid round particles (i.e., spatters).

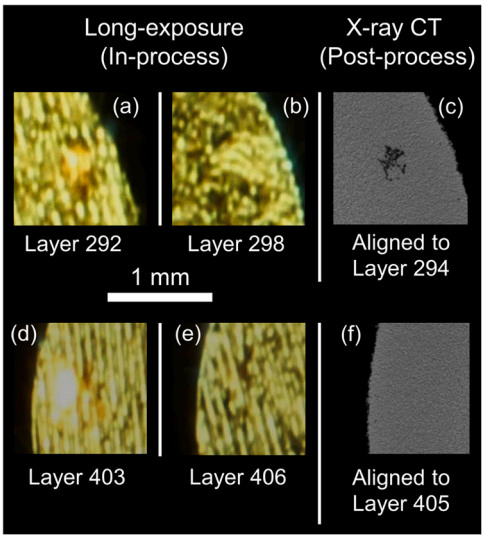

Fig. 4. Comparison between in-process long-exposure events and the corresponding region of the post-process CT volume. From left to right: orange spot, scan tracks and aligned CT cross-section for an outlier event leading to a lack-of-fusion defect (a-c) and for an outlier event not leading to any internal defect (d-f). Orange spots might be slightly shifted in the *x-y* plane, due to perspective correction of deposited spatter particles protruding from the powder bed.

(ROI) including an orange spot is reported in Fig. 5, while the main steps of the algorithm are shown in the workflow of Fig. 6.

After a first rough segmentation for separating the sample layer from the background, the process signatures have to be identified. As can be seen in Fig. 4a and d, these process signatures are often characterized by an outer orange crown circumscribing an inner white core, which is related to an increased pixel saturation due to high-intensity values. Furthermore, these signatures are often surrounded by a darker low-brightness area. Hence, this recurrent pattern is exploited by leveraging the capabilities offered by working in the *HSV* colour space, with the *H-channel* used to segment the orange crown and the *S-channel* to segment the core of the signatures and the surrounding darker region. An example of the outcome obtained by implementing the segmentation procedure is shown in Fig. 6b.

Starting from this preliminary segmentation of the spatter-related process signatures, a region of interest including the potential defect site is created and applied as a mask to the corresponding location in the long-exposure images of subsequent layers (see Fig. 6c).

Fig. 6c also shows that the scan tracks within the ROIs are characterized by high brightness values, which allows exploiting the *V-channel* to segment the tracks (see Fig. 6e) after a pre-processing contrast enhancement (see Fig. 6d). Once the scan tracks corresponding to a specific process signature have been segmented, a skeletonization is performed by morphological erosion using the *bwskel* built-in MATLAB function, see Fig. 6f. This step allows collapsing each scan track into a single line of pixels, whose spatial coordinates can be retrieved and stored. Therefore, the *x-y* coordinates of each scan track were used as input data to carry out both a linear and a second-degree polynomial regression, with the related calculation of the coefficient of determination (r^2) for both cases. Fig. 7 shows the comparison of the linear and the second-degree polynomial fitting performed on a straight and a curved scan track, respectively.

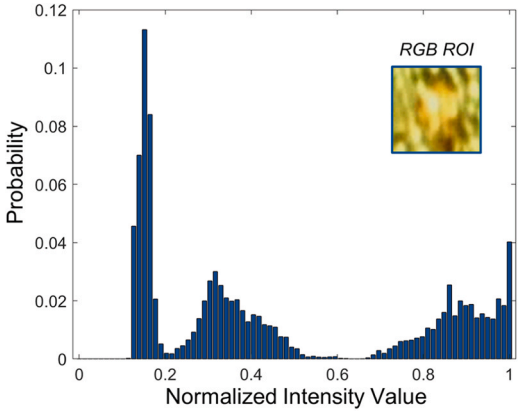

Fig. 5. Histogram of a normalized region of interest including an orange spot, after converting the image to the HSV domain. The orange spot ROI is shown in the RGB domain for visualization purposes.

As can be seen, the difference between the linear and the polynomial r^2 coefficients is much higher in the case of the curved scan track. Therefore, based on Eq. (1), the difference between the two coefficients of determination can be calculated:

$$\Delta r^2 = r^2_{polynomial} - r^2_{linear} \tag{1}$$

Starting from Eq. (1), the following combined condition was imposed to categorize a scan track as potentially defective.

$$\begin{cases} \Delta r^2 > th_1 \\ r^2_{polynomial} > th_2 \end{cases} \tag{2}$$

The specific threshold values, th_1 and th_2, were determined within an optimization framework. Initial values were set based on observed experimental cases that were potentially related to actual defects, and then refined by monitoring the model's performance. The optimized values for th_1 and th_2 converged around 0.1 and 0.9, respectively. Specifically, the first threshold helps distinguish linear from curved scan tracks, while the second ensures that the fitted track is truly curved, filtering out cases where scan tracks segmentation led to entangled tracks.

As for the number of consecutive layers considered, some tracks significantly deviating from straightness were observed up to 7 layers above the process signature detected in the first place (i.e., at '*layer 0*'), which is coherent with previous considerations regarding spatters' dimensions [12]. Consequently, the performance of the analytical model was evaluated based on the number of subsequent layers *(k)*, with a maximum of 8 layers considered. Finally, the bunches of following layers analysed in sequence were considered to be leading to lack-of-fusion defects if critical scan tracks were found – i.e., scan tracks satisfying the combined expression of Eq. (2).

3.2. Machine learning-based approach

This section presents a machine learning model developed for the classification of the in-process long-exposure images with CT reference data.

In the context of in-process PBF-LB/M monitoring, AI-based methods are considered to learn complex relations between process dynamics, process parameters and defects. In fact, the vast amount of data generated by in-situ monitoring and X-ray CT can be exploited for model training [29].

To this end, an ML workflow was tailored to the acquired long-exposure data. Specifically, the recognition of in-process signals critical for porosity formation was investigated, and the advantages and limitations compared to the analytical approach are presented in Section 3.1.

The ML workflow starts by storing the information provided by the porosity analysis performed on post-process CT data. In particular, the alignment method described in Section 2.4 is implemented to enable the registration of the in-process image of any layer to the corresponding CT cross-section. By following this approach, the original CT volume space is transformed into an aligned volume space that can be directly

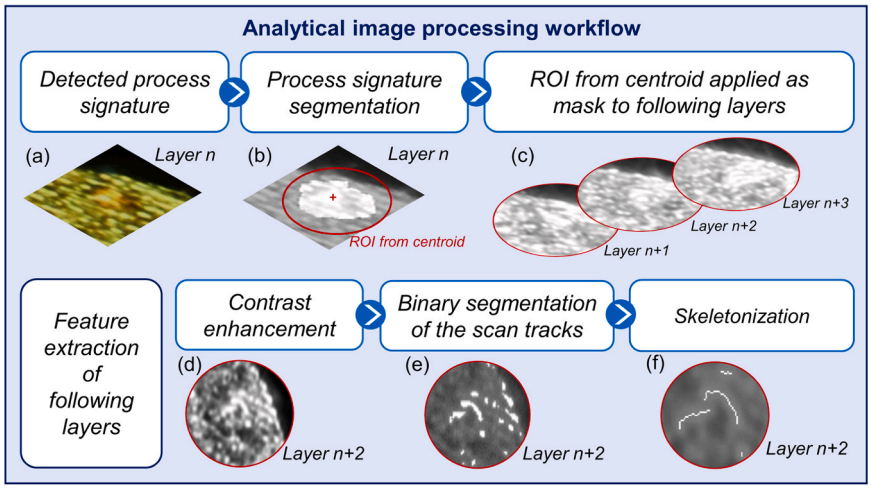

Fig. 6. Main steps of the analytical image processing workflow implemented for extracting the features of interest for the classification of outlier events.

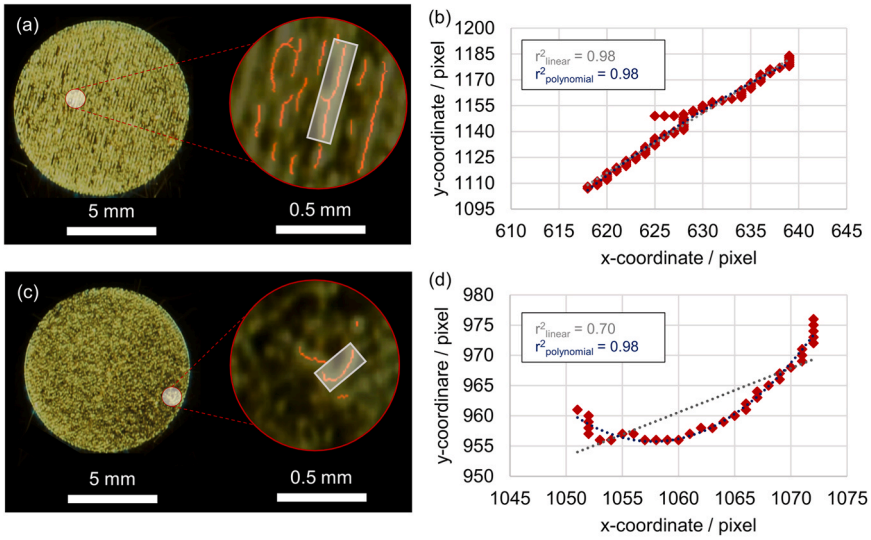

Fig. 7. Linear and polynomial fitting performed on a straight (a) and on a curved (b) scan track.

compared to the in-process monitoring domain [22]. After the alignment, the centroid coordinates of each lack-of-fusion defect within the CT volume were stored in the form of *(x, y, n)*, where *n* represents the layer number and *(x, y)* the in-plane centroid position within the CT cross-section aligned to layer *n*. A region of interest centred on the coordinates stored for each defect was therefore used to include the defect itself in the CT-aligned volume space, as well as potential process signatures in the in-process monitoring domain. A number of material regions equal to the number of stored porous regions were also sparsely identified within the CT volume. This allows creating a balanced dataset between the two classes of interest (i.e., pore and material), reducing the risk of training biased models. At this point, the regions of interest identified in long-exposure images can be related to the corresponding labels generated from reference CT data, which result in either defective or non-defective regions, thus leading to a binary classification problem.

Although the PBF-LB/M process is inherently affected by internal defects, the number of occurrences is often not sufficient for adequately training complex models based on deep convolutional neural networks. On the contrary, simpler machine learning classifiers can perform well even with smaller datasets. A hybrid approach inspired by Liu et al. [30] was implemented in this work. Specifically, convolutional layers are leveraged for the extraction of relevant features from the long-exposure images acquired in-process, while a machine learning classifier was deployed starting from the identified features for the final process signature classification. The overall architecture of the applied model, implemented in Python 3.10 using the TensorFlow framework, is outlined in Fig. 8. The structure of the feature extraction module is detailed in Appendix A.

As can be seen in Fig. 8, the input data consists of regions of interest in the long-exposure images. Each bunch of input ROIs is associated with its corresponding label, obtained from CT reference data as described previously, and therefore essential for training the model following a supervised machine learning approach. In particular, the first ROI relates to the first layer (layer *n* in Fig. 8) showing a process signature (i.e., an orange spot), while the other ROIs are extracted with the same *(x, y)* position across the following layers. The feature extraction module, mainly consisting of convolutional and max pooling layers, is applied to the ROIs to perform the feature extraction, which defines the input data for the classification model. Examples of extracted features are shown in Fig. 9 for two ROIs obtained from following layers.

A preliminary investigation on the data correlation, performed using a logistic regression classifier, is documented in [31]. However, the model architecture was subsequently developed by testing other classification algorithms, with the random forest model achieving better performances in terms of prediction accuracy. Hence, Fig. 8 illustrates the structure of the random forest, implemented using the scikit-learn

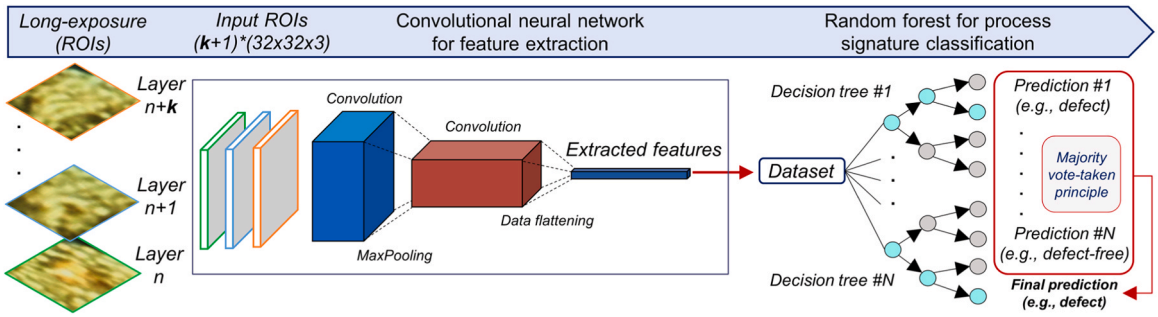

Fig. 8. Schematic representation of the applied machine learning workflow.

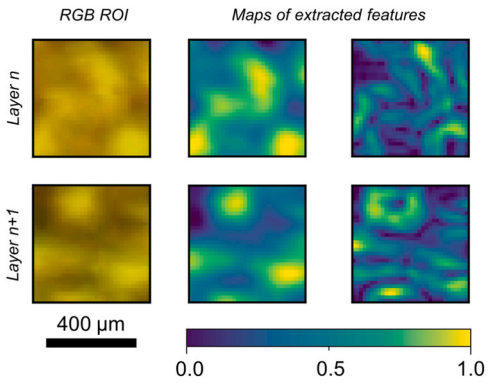

Fig. 9. Example of feature maps obtained after applying the first two convolutional layers on two consecutive ROIs (related to layers *n* and *n+1* and shown in the first and second row, respectively).

library, applied to the binary classification problem based on features extracted from the in-process data.

As reported in Fig. 8, squares with a 32-pixels edge length were selected as ROIs, which corresponds to a length of 480 µm considering the 15 µm pixel size. Therefore, a wide dimensional range of process signatures is captured within the ROIs.

Eighty percent of the dataset, which included all fabricated samples, was used for training and validation, following a 10-fold cross-validation approach. Specifically, this dataset was constructed by selecting 80 % of both defect-related and non-defect-related regions of interest, ensuring a balanced set. This strategy ensures that the model learns features from both classes equally, improving its ability to detect defects effectively. The remaining 20 % constituted the testing set, which, due to the large number of induced spatter-related lack-of-fusion defects, also maintained the same balance between classes. In cases where the number of defects is lower and the dataset imbalanced, the same model can still be applied by tuning its classification threshold to minimize false positives, as discussed in Section 4.2.

Furthermore, the data split among training, validation and testing set was carried out to achieve similar distributions in terms of defect dimension, with each subset being representative of the entire defect population. A grid search approach was implemented to determine the optimal hyperparameter values, with cross-validation used to evaluate the performance of each configuration. The grid search optimized the number of decision trees and the maximum depth of each tree. Based on the cross-validation results, the optimal number of trees was found to be 160, and the maximum depth of the trees was set to 15. Additionally, the minimum number of samples required to split an internal node was tuned, with a value of 5 yielding the best performance across the 10 cross-validation folds. After optimizing the hyperparameters, the model was trained from scratch on the training set and subsequently evaluated for its prediction performance on the testing set.

The impact of considering different values for the parameter *k*, which represents the number of layers following the first appearance of the process signature considered by the model, was evaluated by tracking four main classification metrics: prediction accuracy, precision, recall and F1-score. Prediction accuracy is the most frequently adopted metric, but it consists of a global value that might not be fully representative of the actual performances [32]. Additional information is hence obtained by computing precision and recall, as high precision values are related to low false positive rates, while high recall values can be linked to low false negative rates. The F1-score is a summary metric of precision and recall, balancing both aspects of the model performances. In an ideal case, it should be equal to *1*.

4. Experimental results

The present section documents the performance obtained for defects classification in the two different scenarios of the analytical approach based on image processing and of the ML-based workflow, respectively in Sections 4.1 and 4.2. Advantages and limitations of the two approaches are discussed in Section 4.3.

4.1. Performances of the analytical approach for defects classification

The performances achieved for defects classification by the analytical image processing approach, based on the scan tracks curvature identification described in Section 3.1, were evaluated by tracking the same metrics used for the machine learning workflow (accuracy, precision, recall and F1-score), which include insights on both false positives and false negatives as described in Section 3.2.

Fig. 10a represents how the model performances vary when considering different numbers of layers after the process signature identification, for defects with a diameter down to 90 µm. As previously stated in Section 3.1, curved tracks were identified up to 7 layers above the detected signature for the cases investigated in this work. In support of this observation, the model performances improve for an increasing number of analysed layers, with better metrics (accuracy, recall, and F1-score) achieved when analysing 7 subsequent layers. The precision value, instead, stays above 80 % in each of the analysed cases, which comes at the expense of lower recall rates. A higher precision means that the false positive rate is lower, which can be interpreted as a low tendency of the model to wrongly classify as porosity a process signature not actually linked to any defect. On the other hand, a low recall implies that the model is affected by high false negative rates, which leads to a significant probability of missing the identification of critical process signatures. This can be due to the following reasons: (i) the criteria defined in Eq. (2), to identify curved tracks of interest and corresponding critical process signatures can be too severe for some defective regions; (ii) some local regions in the layer-wise images were observed to be characterized by slightly different light reflections, which can influence the scan track detection; (iii) some regions of layers above a process signature do not show any curvature in the scan tracks, despite resulting in actual defects.

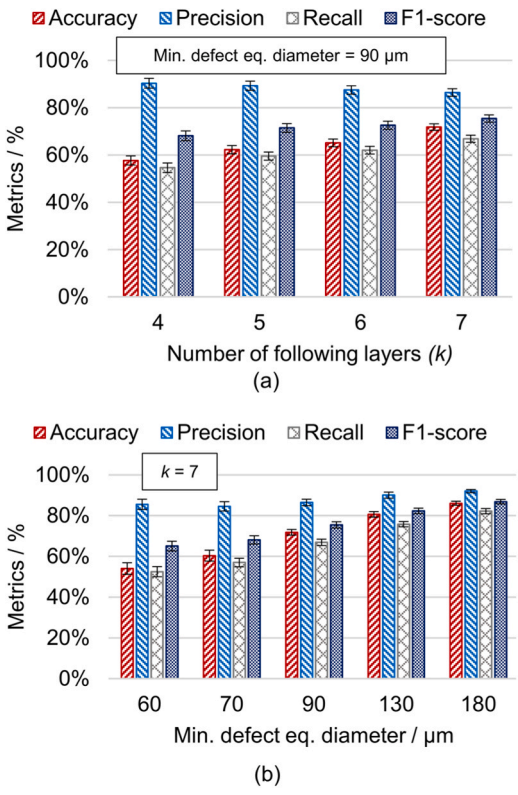

Fig. 10. Performance of the image processing algorithm based on the scan tracks curvature. Metrics values against the number of following layers considered (a) and against the minimum defect equivalent diameter (b). Error bars represent ±1 standard deviation.

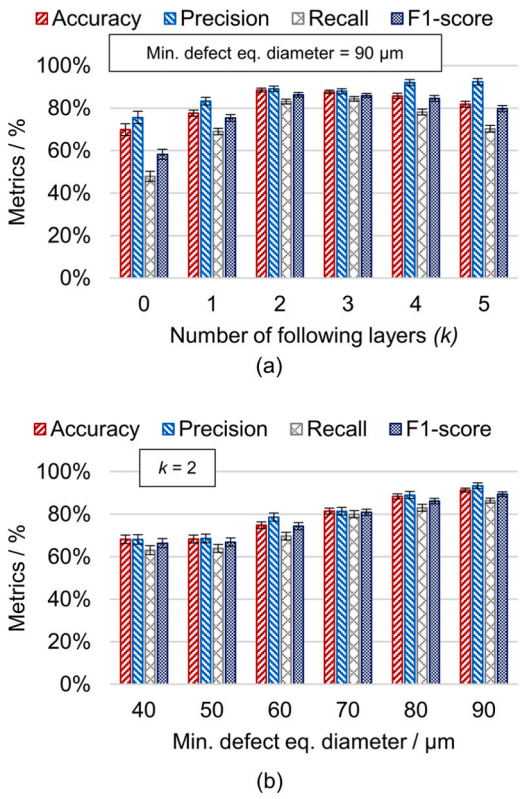

Fig. 11. Performance of the machine learning model evaluated by varying the number of following layers for feature extraction (a) and by considering different minimum defect equivalent diameters (b). Error bars represent ±1 standard deviation.

Fig. 10b shows how the model performances vary for different minimum defect equivalent diameters, when considering 7 layers for the prediction. The recall value becomes acceptable (i.e., above 70 %) for a minimum equivalent diameter of 90 μm. The overall model performances quickly decrease for smaller minimum defect diameters. This suggests that small defects are caused by smaller spatter particles, with less probability of altering the powder bed and provoking significant straightness deviations of the scan tracks. As a further confirmation of this finding, the metrics range between 80 % and 90 % registered for defects above 180 μm in diameter.

4.2. *Performances of the machine learning approach for defects classification*

The performances achieved by means of the developed machine learning architecture are presented in Fig. 11. Fig. 11a compares the ML model performances for a given minimum defect diameter of 90 μm by considering different values for the parameter k defined in Fig. 8. As can be seen, an accuracy of about 70 % and a recall of around 48 % are obtained by analysing only the layer where the process signature is detected. The very small recall value implies that the model has a high false negative prediction rate, which means it tends to fail the identification of process signatures leading to the generation of actual pores. It is important to note that the reference CT data becomes fundamental when only one layer from the in-process domain is considered. However, considering the metrological approach for achieving accurate high-resolution CT scans and the related data alignment methodology, the probability of accurately correlating defects larger than 50 μm with corresponding regions in the CT domain has been shown to be over 90 % [22].

The model performances significantly improve for increasing k values, showing a peak for k equal to 2 and 3. In particular, in the case of $k = 2$, the model accuracy is slightly below 90 % and the F1-score exceeds 85 %. Precision and recall are both between 80 % and 90 %, confirming that both false positive and negative rates are reduced. Furthermore, Fig. 11a also shows that, for defects with a minimum equivalent diameter of around 90 μm, including more than 4 layers in the analysis leads to slightly worsened overall performances. This might be caused by the increased number of extracted features feeding the random forest classifier, which implies an increased complexity of the input data that have to be processed by the model.

Fig. 11b represents the performance of the proposed model architecture considering the information of two following layers when dealing with lack-of-fusion defects characterized by different minimum diameters. As can be seen, there is an increasing trend of the performances for increasing minimum defect diameters, indicating that the prediction accuracy is higher for larger defects. In particular, the evaluated metrics show values around 65 % for defects below 50 μm, and significantly higher values for defects above 70 μm in equivalent diameter.

To evaluate the performance of the machine learning model across various classification thresholds, the receiver operating characteristic (ROC) curves and the corresponding area under the ROC curve (AUC) values were computed. The ROC curves provide a comprehensive view of the model's ability to distinguish between defective and non-defective regions by plotting the true positive rate against the false positive rate for different threshold values.

Fig. 11 shows results obtained using the default threshold value of 0.5 for the random forest classifier. The AUC, on the other hand, provides a threshold-independent measure of the model's overall performance, with higher AUC values indicating better model ability to separate between the two classes.

As can be seen in Fig. 12a for the case of minimum defect equivalent diameter of 90 μm, the ROC curves obtained for increasing k values from

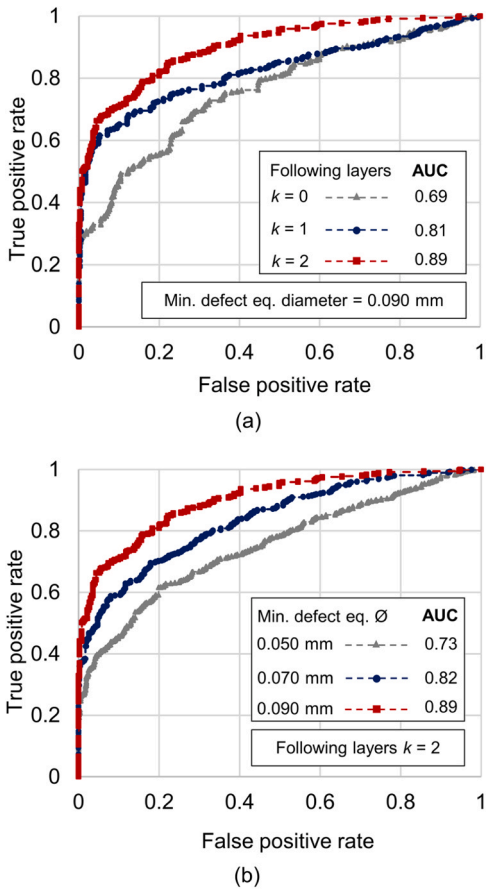

Fig. 12. Performances of the machine learning model through the computation of the *ROC* curves and *AUC* values by considering different values of *k* (a) and by varying the minimum defect equivalent diameter (b).

0 to 2 lead to larger AUC values. This aspect confirms the positive impact of analysing also the subsequent layers for the discrimination of false positives. Specifically, the best AUC of 0.89 is obtained for *k* equal to 2, with a 30 % improvement with respect to *k* equal to 0 and 10 % with respect to *k* equal to 1.

As already mentioned in Section 3.2, the model might potentially be applied in scenarios where defects are much rarer than in experimental cases investigated in this work. High AUC values, such as those achieved by considering following layers, imply the feasibility of adapting the model to cases with lower defect densities, without requiring re-training.

Fig. 12b shows the *ROC* curves and *AUC* values computed for *k* equal to 2 and for defects of different diameters. In this case, it is clear how the model is better at correctly classifying large defects, since higher false positive rates resulted while considering smaller defects. In fact, for a false positive rate equal to 0.2, more than 80 % of regions leading to lack-of-fusion defects are correctly classified in case of defects with a minimum equivalent diameter equal to or above 90 μm. On the contrary, this true positive rate decreases to 70 and 60 % for defects with minimum diameters equal to or above 70 μm and 50 μm. While high AUC values achieved in the prediction of larger defects show promise with reference to model adaptation to different defect density scenarios, lower values obtained on smaller defects, such as those below 70 μm in equivalent diameter, also imply a reduced model adaptability.

4.3. Discussion on the comparison between the two approaches

As it can be seen by comparing the classification metrics shown in Figs. 10 and 11, the machine learning approach appears to perform better than the analytical image processing approach, both in terms of minimum dimension of defects classified with an adequate level of confidence, and in terms of number of layers to be analysed to take the classification decision. The latter aspect is fundamental to reducing the time needed to apply corrective actions in real-time.

Fig. 13 shows a three-dimensional representation of a number of defects contained in the testing dataset. More specifically, Fig. 13a shows the positioning of these defects within a CT volume for visualization purposes, while Fig. 13b reports the prediction performances of each model in the in-process regions corresponding to the considered defects. As can be seen, the majority of smaller defects are correctly predicted by the machine learning model, but not by the analytical method as shown in the histogram of Fig. 10. Regarding larger defects, both models show a good prediction rate. However, it is worth noting that in the subset of the testing dataset represented in Fig. 13, a large lack-of-fusion defect (represented in dark orange colour in the inset of Fig. 13a), was not predicted by the machine learning model, but properly predicted by the analytical approach. This particular defect can be linked to the presence of a spatter particle, as confirmed by its peculiar shape, as well as by the orange spot visible in the inset (orange box) of Fig. 13b.

Therefore, the two approaches are not mutually exclusive, and a higher confidence level could be achieved by combining them in the prediction of lack-of-fusion defects caused by spatters. A significant number of defects can be predicted in a short time (i.e., within two layers) exploiting the machine learning approach, while some of the defects not identified could be predicted in a longer time (e.g., within seven layers) by the analytical approach, further improving the probability of a proper defect classification. Contradictory prediction results between the two methods can be addressed by assigning more weight to the ML-based predictions for smaller defects, while doing the opposite for larger defects where scan tracks are properly detected by the analytical approach.

As a further remark, the analytical method has proven effective in layers produced with a meander strategy, but separate tests on chessboard scan strategies revealed limitations in areas where adjacent chess patterns intersect. Defect formation predictions in such regions can however be tackled with the ML-based methodology, further emphasizing the potential of combined approaches.

The study of combined implementations of the two proposed approaches is planned for investigation in future developments of this research.

5. Conclusions

This work presented two different approaches – analytical and ML-based – for analysing in-process laser powder bed fusion monitoring data acquired using the off-axis long-exposure imaging technique, which is a cost-effective and machine-agnostic monitoring solution. In particular, the proposed methods were focused on assessing the chance of predicting the occurrence of lack-of-fusion defects caused by spatter particles from data gathered in-process. Results demonstrated the need to consider multiple layers of data for accurately predicting the formation of spatter-related internal defects. Good prediction capabilities were observed when using long-exposure monitoring, depending on the defect size. This paves the way for effective machine integration of this monitoring solution and the related algorithms.

As outcomes of the work, the following main conclusions can be drawn for the analytical approach, which is based on the detection and measurement of scan track curvature induced by spatter particles:

- Good prediction accuracies were achieved for defects above 130 μm, when analysing seven layers following the process signature identification.
- The criteria based on the in-process measurement of scan track curvatures has proved to be a viable option for the discrimination

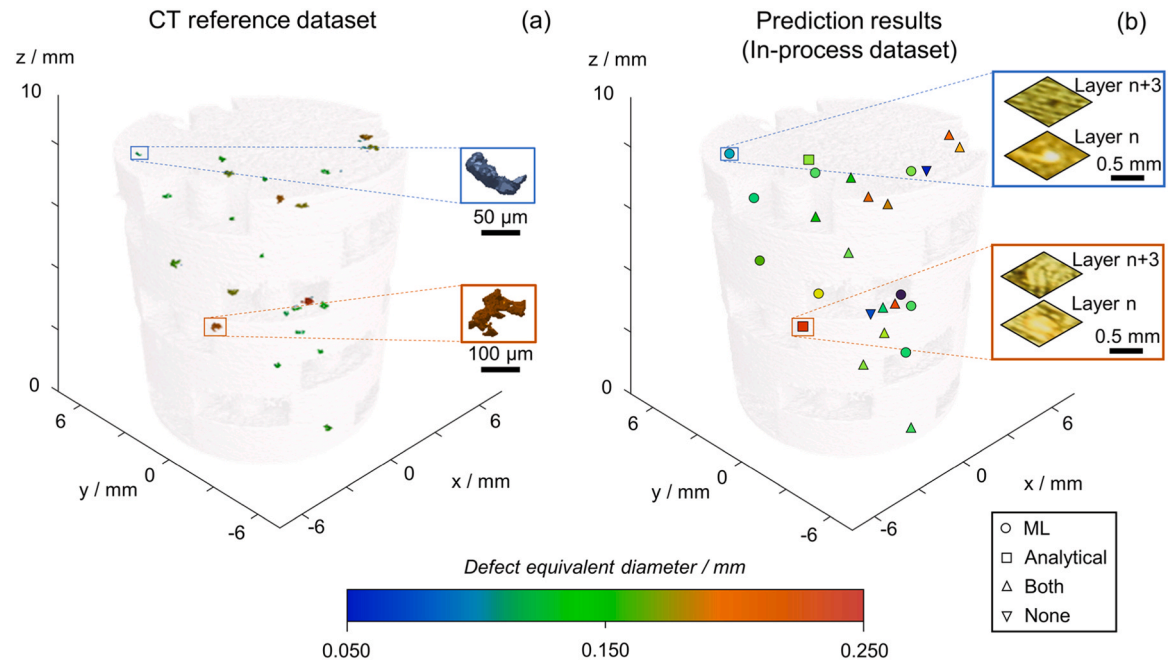

Fig. 13. Subset of the testing set represented within a CT reconstructed volume (a); Prediction results of the analytical and the ML model on each in-process location corresponding to the considered defects, superimposed to the same CT volume for the sake of an easier interpretation (b). The colours assigned in both figures are linked to the equivalent diameter of each defect.

between false and true positives in images acquired using the off-axis long-exposure monitoring technique.

- Data acquired using a single camera, as in the present work, led to challenges in the scan track curvature identification due to different reflections generated by tracks with diverse relative orientations with respect to the direction of sight. Future work will explore the use of multiple cameras to enhance the scan track assessment, since multiple viewpoints are expected to provide a clearer view of the scan tracks, regardless of their orientation within the layer.

Similarly, the following main outcomes results from application of the developed machine learning modelling approach:

- The methodology, based on combining image convolutions with ML classifiers, has proved to be effective in learning significant patterns from long-exposure images acquired during the PBF-LB/M process.
- Studying the correlation of in-process gathered data of single layers to CT porosity reference data was found not sufficient to predict spatter-related defects, despite performing an accurate data alignment. This was confirmed by prediction accuracy and F1-score values around 70 % and below 60 %, respectively, for defects with an equivalent diameter equal to or greater than 90 µm.
- On the other hand, considering data from multiple and consecutive in-process layers resulted fundamental for performing accurate porosity predictions. Indeed, performance metrics improved significantly with two or three subsequent layers, achieving values of prediction accuracy and F1-score between 80 % and 90 % for defects with equivalent diameter above 80 µm.
- The model's ability to categorize potentially defective regions within two subsequent layers demonstrates good earliness, allowing for quick actions under feedback control. However, AI solutions can lack interpretability compared to analytical approaches, with slightly different in-process patterns possibly leading to incorrect predictions. Planned research activity aims at combining ML and analytical approaches to enhance prediction confidence, thus reducing the risk of missing dangerous defects.

Future works will focus on improving the detection and prediction of smaller defects by addressing the resolution limits of off-axis solutions. This will involve investigating the benefits of multi-sensor data fusion, combining off-axis long-exposure imaging with co-axial cameras or photo-diodes to cover a wider range of defect sizes. Additionally, the range of classification methods will be extended, exploring the use of neural networks for potential improvements when trained on large datasets. The developed approaches will also be tested on industrial components and various materials to assess their effectiveness in different contexts.

CRediT authorship contribution statement

Nicolò Bonato: Writing – review & editing, Writing – original draft, Visualization, Validation, Software, Methodology, Investigation, Formal analysis, Data curation, Conceptualization. **Simone Carmignato:** Writing – review & editing, Validation, Supervision, Methodology, Data curation, Conceptualization. **Filippo Zanini:** Writing – review & editing, Writing – original draft, Visualization, Validation, Methodology, Investigation, Funding acquisition, Data curation, Conceptualization.

Declaration of Competing Interest

The authors declare that they have no known competing financial interests or personal relationships that could have appeared to influence the work reported in this paper.

Acknowledgements

The work received funding from project BIRD222741/22 (UNIPD). The authors would like to acknowledge Mr. Luca Bernardi for his valuable contribution to the experimental part of the work.

Appendix A. Feature extractor module

Layer	Number of filters	Kernel size	Activation	Output shape
Conv2d	32	(3, 3)	sigmoid	(32, 32, 32)
BatchNorm2d	/	/	/	(32, 32, 32)
Conv2d	32	(3, 3)	sigmoid	(32, 32, 32)
BatchNorm2d	/	/	/	(32, 32, 32)
MaxPooling2d	/	2×2	/	(32, 16, 16)
Conv2d	64	(3, 3)	sigmoid	(64, 16, 16)
BatchNorm2d	/	/	/	(64, 16, 16)
Conv2d	64	(3, 3)	sigmoid	(64, 16, 16)
BatchNorm2d	/	/	/	(64, 16, 16)
MaxPooling2d	/	2×2	/	(64, 8, 8)

Data availability

Data will be made available on request.

References

[1] M. Schmidt, et al., Laser based additive manufacturing in industry and academia, CIRP Ann. 66 (2) (2017) 561–583, https://doi.org/10.1016/j.cirp.2017.05.011.

[2] H. Gong, et al., Analysis of defect generation in Ti–6Al–4V parts made using powder bed fusion additive manufacturing processes, Addit. Manuf. 1-4 (2014) 87–98, https://doi.org/10.1016/j.addma.2014.08.002.

[3] A.N.D. Grasper, et al., Spatter and oxide formation in laser powder bed fusion of Inconel 718, Addit. Manuf. 24 (2018), https://doi.org/10.1016/j.addma.2018.09.032.

[4] E. Wycisk, et al., Fatigue performance of laser additive manufactured Ti–6Al–4V in very high cycle fatigue regime up to 10^9 Cycles, Front. Mater. 2 (2015), https://doi.org/10.3389/fmats.2015.00072.

[5] G. Tapia, A. Elwany, A review on process monitoring and control in metal-based additive manufacturing, ASME J. Manuf. Sci. Eng. 136 (6) (2014), https://doi.org/10.1115/1.4028540.

[6] M. Mani, et al., Measurement science needs for real-time control of additive manufacturing powder bed fusion processes, NIST Interag. Intern. Rep. 8036 (2015) 629–652, https://doi.org/10.6028/NIST.IR.8036.

[7] V. Renken, et al., Development of an adaptive, self-learning control concept for an additive manufacturing process, CIRP J. Manuf. Sci. Technol. 19 (2017) 57–61, https://doi.org/10.1016/j.cirpj.2017.05.002.

[8] M. Grasso, et al., In-situ measurement and monitoring methods for metal powder bed fusion: an updated review, Meas. Sci. Technol. 32 (2021) 112001, https://doi.org/10.1088/1361-6501/ac0b6b.

[9] L. Scime, et al., Layer-wise anomaly detection and classification for powder bed additive manufacturing processes: a machine-agnostic algorithm for real-time pixel- wise semantic segmentation, Addit. Manuf. 36 (2020) 101453, https://doi.org/10.1016/j.addma.2020.101453.

[10] L. Pagani, et al., Automated layerwise detection of geometrical distortions in laser powder bed fusion, Addit. Manuf. 36 (2020), https://doi.org/10.1016/j.addma.2020.101435.

[11] J. Bamberg, et al., In-process control of selective laser melting by quantitative optical tomography, 19th World Conf. Non-Destr. Test. (2016), https://doi.org/10.1111/jocn.13165.

[12] C. Schwerz, et al., In-situ detection of redeposited spatter and its influence on the formation of internal flaws in laser powder bed fusion, Addit. Manuf. 47 (2021), https://doi.org/10.1016/j.addma.2021.102370.

[13] Z. Snow, et al., Observation of spatter-induced stochastic lack-of-fusion in laser powder bed fusion using in situ process monitoring, Addit. Manuf. 61 (2023) 103298, https://doi.org/10.1016/j.addma.2022.103298.

[14] G. Mohr, et al., In-Situ Defect Detection in Laser Powder Bed Fusion by Using Thermography and Optical Tomography—Comparison to Computed Tomography, Metals 10 (2020), https://doi.org/10.3390/met10010103.

[15] J.B. Forien, et al., Detecting keyhole pore defects and monitoring process signatures during laser powder bed fusion: a correlation between in situ pyrometry and ex situ X-ray radiography, Addit. Manuf. 35 (2020) 101336, https://doi.org/10.1016/j.addma.2020.101336.

[16] Z. Smoqi, et al., Monitoring and prediction of porosity in laser powder bed fusion using physics-informed meltpool signatures and machine learning, J. Mater. Process. Technol. 304 (2022) 117550, https://doi.org/10.1016/j.jmatprotec.2022.117550.

[17] L. Scime, et al., Using machine learning to identify in-situ melt pool signatures indicative of flaw formation in a laser powder bed fusion additive manufacturing process, Addit. Manuf. 25 (2019) 151–165, https://doi.org/10.1016/j.addma.2018.11.010.

[18] H. Baumgartl, et al., A deep learning-based model for defect detection in laser-powder bed fusion using in-situ thermographic monitoring, Prog. Addit. Manuf. 5 (2020) 277–285, https://doi.org/10.1007/s40964-019-00108-3.

[19] Z. Snow, et al., Toward in-situ flaw detection in laser powder bed fusion additive manufacturing through layerwise imagery and machine learning, J. Manuf. Syst. 59 (2021) 12–26, https://doi.org/10.1016/j.jmsy.2021.01.008.

[20] B. Kavas, et al., Layer-to-layer closed-loop feedback control application for inter-layer temperature stabilization in laser powder bed fusion, Addit. Manuf. 78 (2023), https://doi.org/10.1016/j.addma.2023.103847.

[21] R.K. Leach, et al., Geometrical metrology for metal additive manufacturing, CIRP Ann. 68 (2) (2019) 677–700, https://doi.org/10.1016/j.cirp.2019.05.004.

[22] N. Bonato, F. Zanini, S. Carmignato, Deformations modelling of metal additively manufactured parts and improved comparison of in-process monitoring and post-process X-ray computed tomography, Addit. Manuf. 75 (2023), https://doi.org/10.1016/j.addma.2023.103736.

[23] Bonato N., et al (2022). On the alignment of in-process and post-process measurement datasets acquired for precision enhancement of laser powder bed fusion of metals. Euspen 22nd International Conference and Exhibition, Geneva (CH). 2-s2.0-85145581987.

[24] ISO 286-1, Geometrical product specifications (GPS) - ISO code system for tolerances on linear sizes - Basis of tolerances, deviations and fits, International Organization for Standardization, Geneve, 2010.

[25] F. Zanini, N. Bonato, S. Carmignato, New multi-function building plate for improving metal laser powder bed fusion by enhancing the accuracy and alignment of in-process monitoring and computed tomography data, Int. J. Adv. Manuf. Technol. (2024), https://doi.org/10.1007/s00170-024-13514-x.

[26] A. Charles, et al., Elucidation of dross formation in laser powder bed fusion at down-facing surfaces: phenomenon-oriented multiphysics simulation and experimental validation, Addit. Manuf. 50 (2022) 102551, https://doi.org/10.1016/j.addma.2021.102551.

[27] R. Esmaeilizadeh, et al., On the effect of spatter particles distribution on the quality of Hastelloy X parts made by laser powder-bed fusion additive manufacturing, J. Manuf. Process. 37 (2019) 11–20, https://doi.org/10.1016/j.jmapro.2018.11.012.

[28] F. Caltanissetta, et al., Characterization of in-situ measurements based on layerwise imaging in laser powder bed fusion, Addit. Manuf. 24 (2018) 183–199, https://doi.org/10.1016/j.addma.2018.09.017.

[29] T. Herzog, et al., Process monitoring and machine learning for defect detection in laser-based metal additive manufacturing, J. Intell. Manuf. (2023), https://doi.org/10.1007/s10845-023-02119-y.

[30] Y.H. Liu, Feature extraction and image recognition with convolutional neural networks, J. Phys.: Conf. Ser. 1087 (2018) 062032, https://doi.org/10.1088/1742-6596/1087/6/062032.

[31] Bonato, N., Zanini, F., Carmignato, S. (2024). Investigation on the use of machine learning and X-ray computed tomography for lack-of-fusion porosity prediction. ASPE Summer Topical Meeting, Golden (CO).

[32] M. Hossin, Sulaiman M.N, A review on evaluation metrics for data classification evaluations, Int. J. Data Min. Knowl. Manag. Process 5 (2015), https://doi.org/10.5121/ijdkp.2015.5201.